A new method for reconstruction of the structure of micro-packed beds of spherical particles from desktop X-ray microtomography images. Part A. Initial structure generation and porosity determination

M. Navvab Kashani,[1] V. Zivkovic,[2] H. Elekaei,[1] M.J. Biggs[1,3*]

1. School of Chemical Engineering, The University of Adelaide, SA 5005, Australia.

2. School of Chemical Engineering and Advanced Materials, Newcastle University, Merz Court, Newcastle-upon-Tyne, NE1 7RU, UK.

3. School of Science, Loughborough University, Loughborough, LE11 3TU, UK.

Abstract

Micro-packed beds (µPBs) are seeing increasing use in the process intensification context (*e.g.* micro-reactors), in separation and purification, particularly in the pharmaceutical and bio-products sectors, and in analytical chemistry. The structure of the stationary phase and of the void space it defines in such columns is of interest because it strongly influences performance. However, instrumental limitations – in particular the limited resolution of various imaging techniques relative to the particle and void space dimensions – have impeded experimental study of the structure of µPBs. We report here a new method that obviates this issue when the µPBs are composed of particles that may be approximated by monodisperse spheres. It achieves this by identifying in successive cross-sectional images of the bed the approximate centre and diameter of the particle cross-sections, replacing them with circles, and then assembling them to form the particles by identifying correlations between the successive images. Two important novel aspects of the method proposed here are it does not require specification of a threshold for binarizing the images, and it preserves the underlying spherical geometry of the packing. The new method is demonstrated through its application to a packing of a near-monodispersed 30.5 µm particles of high sphericity within a 200 µm square cross-section column imaged using a machine capable of 2.28 µm resolution. The porosity obtained was, within statistical uncertainty, the same as that determined *via* a direct method whilst use of a commonly used automatic thresholding technique yielded a result that was nearly 10% adrift, well beyond the experimental uncertainty. Extension of the method to packings of spherical particles that are less monodisperse or of different regular shapes (*e.g.* ellipsoids) is also discussed.

Keywords: Micro-packed capillary; micro-packed bed; process intensification; porosity; X-ray microtomography; thresholding.

---

[*] m.biggs@lboro.ac.uk

1. Introduction

Micro-packed beds (μPBs) are seeing increased use as miniaturization of processes becomes more prevalent. For example, they provide a means of greatly enhancing mixing and, thus, heat and mass transfer in the laminar flows that are inevitable in the microchannels encountered in process intensification (Hotz et al., 2008, Mills et al., 2007, Ajmera et al., 2001, Jensen, 2001, Losey et al., 2001). They also bring an increased surface area-to-volume ratio that is useful if the particles within the bed are to act as an adsorbent or catalyst (Kiwi-Minsker and Renken, 2005, Oleschuk et al., 2000). The small test volumes and short residence times also make μPBs ideal for rapid, high-throughput catalyst screening (Cao et al., 2007, Ehrfeld et al., 2000), and in the liquid chromatography context in the pharmaceutical sector (Jung et al., 2009). They are also of relevance to micro-fluidized beds (Zivkovic et al., 2013a, Zivkovic et al., 2013b, Doroodchi et al., 2012, Doroodchi et al., 2013) in that they are clearly formed from packed beds. Beyond the process engineering context, μPBs are used in Micro Total Analysis Systems (μTAS), which have long been used for chemical and biochemical analysis (Reyes et al., 2002), including in clinical chemistry (also known as lab-on-a-chip or LOC) (Schulte et al., 2002, Melin and Quake, 2007, Haeberle et al., 2012, Abgrall and Gué, 2007).

Spherical particles are commonly used to form μPBs as they tend to ease the formation of more homogeneous bed structures that are known to give the best heat and mass transfer performance (Aggarwal et al., 2012). Use of smaller particles relative to the microchannel size also improves bed structure homogeneity as well as reduce 'wall effects' (Aggarwal et al., 2012), which lead to the fluid preferentially channelling along the walls rather than passing through the bed. However, as pressure drop and, therefore, pumping power tends to increase as the particle size drops (Unger et al., 2008, Dautzenberg and Mukherjee, 2001, DeStefano et al., 2008), a trade-off in the particle-to-microchannel size must be accepted. In order to assess this trade-off as well as other issues related to the structure of the μPBs, a capacity to gain detailed understanding of the bed structure as a function of the particle characteristics and preparation conditions would be useful.

A variety of techniques have been used to study the structure of μPBs. A number of workers have used scanning electron microscopy (Liang et al., 2003, Motokawa et al., 2002, Dulay et al., 1998) and transmission electron microscopy (Courtois et al., 2006, Plummer et al., 1995). These techniques are, however, tedious to extend to quantitative characterization of the three-dimensional (3D) structure of μPBs. Such analysis is possible using magnetic resonance imaging (MRI) (Man et al., 2005, Sederman et al., 2001), scanning confocal microscopy (Bromley and Hopkinson, 2002), and X-ray microtomography (Williams and Jia, 2003). The last one has the advantage of being able to reveal the transport processes occurring within the pore space in addition to resolving the bed

structure that yields the pore space. It is, however, limited to systems containing protons (*i.e.* either the solid phase or void space must be proton-containing), and requires access to expensive-to-buy and operate machines as well as the expertise to run them. These issues are not faced with scanning confocal microscopy but it can only probe the order of 100 μm or so into media (Claxton et al., 2006). X-ray microtomography offers a balance between the two methods: it can be used to image the entirety of a wide variety of materials, and easy-to-use bench-top systems are now available at modest prices (Fu et al., 2006). This technique has been used in a non-destructive way to study macroscale packed beds (Suzuki et al., 2008, Suzuki et al., 2004), porous tissue scaffolds (Ho and Hutmacher, 2006, Atwood et al., 2004), bone (Jaecques et al., 2004, Jones et al., 2004), stone, rock, minerals and fossils (Ketcham and Carlson, 2001), food products (Lim and Barigou, 2004), and foams (Calvo et al., 2009, Shen et al., 2004) amongst other materials (Salvo et al., 2003).

X-ray microtomography yields a series of planar digital greyscale images along an axis of a sample (*e.g.* along the length of a packed bed). When the size of the pixels in these images is small compared to the characteristic dimensions of the pore space and particles, the underlying geometry (*e.g.* spherical if bed is composed of spheres) is easily discerned. This is, however, not the case for μPBs where the resolution is comparable to the characteristic dimensions – here, instead, a sense of the underlying geometry is largely lost as illustrated in Figure 1, which shows a raw image and its binarized counterpart of a cross-section through a μPB composed of essentially spherical particles. Possible reasons for the compromised CT scans are Poisson noise and beam hardening, which can both produce dark and bright streaks between two high attenuation objects (Boas and Fleischmann, 2012) like spherical glass particles; see Figure1(a). In addition, partial volume and scattered radiation artefacts probably also contributed to the noisy CT scan images seen here (Buzug, 2008).
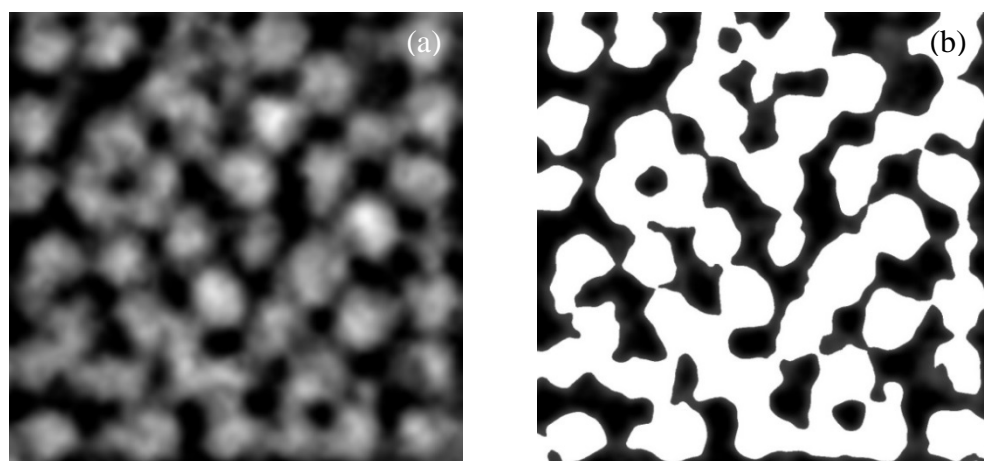

Figure 1. Typical images of a cross-section of a μPB composed of near-monodisperse 30.5 μm diameter particles of high sphericity as derived from X-ray microtomography: (a) raw greyscale image; and (b) a binarized version of the raw image obtained using the Otsu automatic thresholding algorithm.

A second major issue in using typical X-ray microtomography imaging, which is encountered when seeking to reconstruct the 3D structure of µPBs, is the conversion of the grayscale images into their binary counterparts as shown in Figure 1. This requires the identification of the grey level (the 'threshold') that allows the partitioning of the pixels between the solid and void phases (Fajardo et al., 2002, Hara et al., 2002, Ding et al., 1999, Mitton et al., 1998, Al-Raoush and Alshibli, 2006). Many thresholding algorithms have been developed over the years (Sheppard et al., 2004, Waarsing et al., 2004, Ding et al., 1999, Wonho and Lindquist, 1999, Otsu, 1979), reviews for which may be found in (González and Woods, 2008, Sezgin and Sankur, 2004, Pal and Pal, 1993). The plethora of these algorithms reflects the non-trivial nature of finding a threshold, and that there is no single algorithm that is successful for all problems. This threshold-identification issue is more problematic when the pixel size is much smaller than the system characteristic dimensions. However, it becomes a major issue for µPBs where a small change in the threshold leads to significant shifts in pixels from one phase to the other.

Here we propose an approach to constructing 3D models of µPBs of near-spherical particles from X-ray microtomography images of them that avoids the two issues outlined immediately above. The method essentially involves two parts: (A) identifying approximate positions of the particles of the packing, and (B) 'relaxing' the particle packing from the first part using a Reverse Monte Carlo technique combined with simulated annealing. We provide details of the first part in this paper and demonstrate its validity by comparing the porosity obtained from the non-relaxed packing with a directly measured porosity. The second part and its application are outlined in an accompanying paper.

2. Description of the new method

The new method is composed of Part A and Part B; attention here is restricted to Part A, whilst the other part will be detailed in an accompanying paper, referred to as Part B hereafter.Part A is composed of the four steps that are summarized in Figure 2. The first two are applied to all the cross-sectional X-ray microtomographic images obtained along the length of the packing, Figure 2(a). The final two steps involve integration of the data from all the cross-sectional images to form the 3D model. The four steps here have been implemented using the MATLAB Image Processing Toolbox and ImageJ (Rasband, 1997-2013). Integration of the functionality of these two pieces of software was achieved using MIJ, the MATLAB-ImageJ bi-directional communication package (Sage et al., 2012).
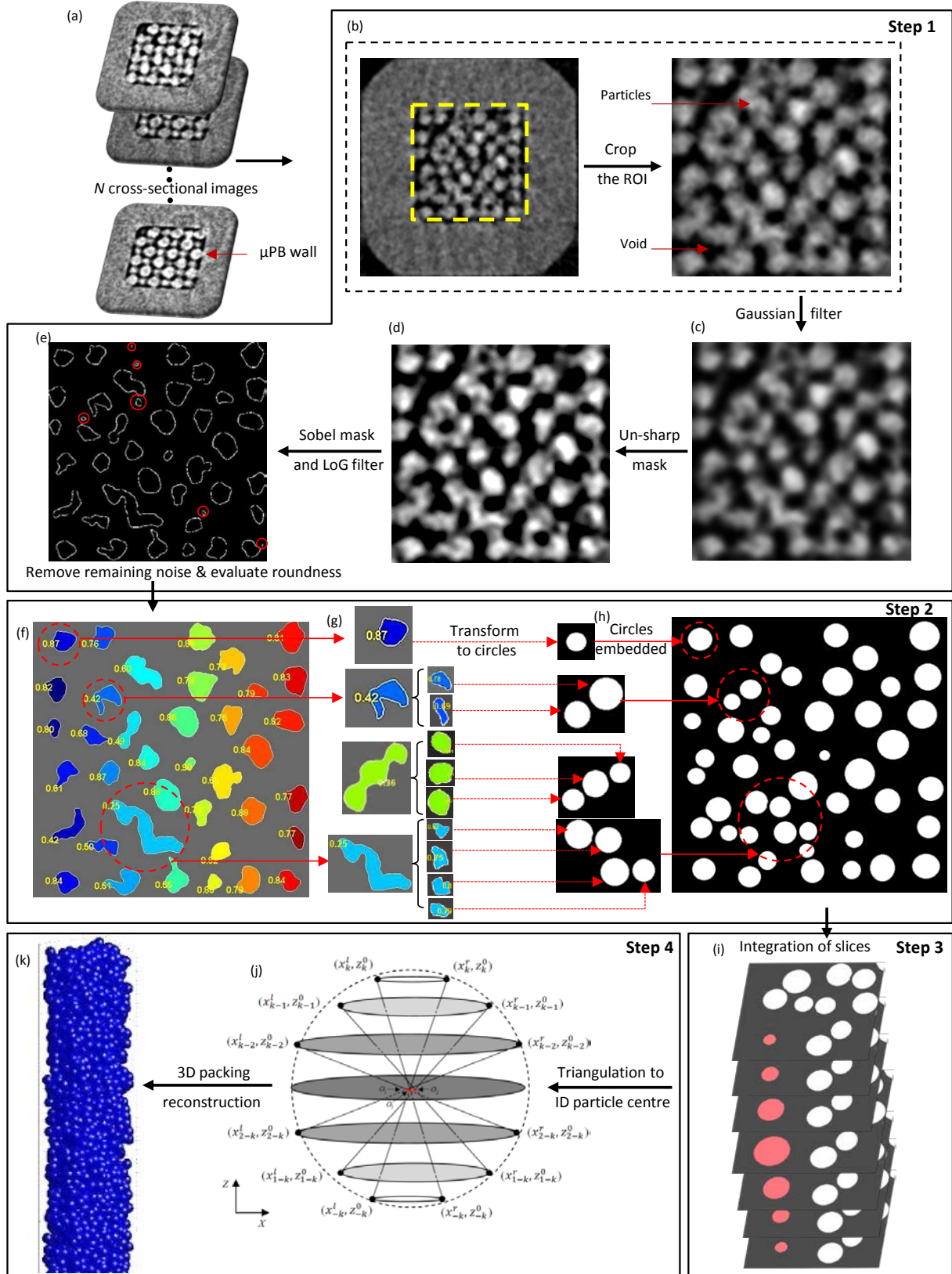
Figure 2. The steps of the new method to construct a 3D model of a μPB from X-ray microtomographic images of the bed.

Step 1. Pre-processing

This step is applied independently to all N cross-sectional images. An image is first cropped to include only the region of interest (ROI), which normally is defined as that area within the µPB walls as illustrated in Figure 2(b). Smoothing is then applied to the image to supress as much noise as possible without destroying the edges of the solid phase; this is done by applying a symmetric 2-dimensional Gaussian filter of 3×3 pixels size and variance 0.5 to the image, Figure 2(b)→(c). An un-sharp mask is then applied to sharpen the edges without overly enhancing any noise remaining in the image (Sheppard et al., 2004) as shown in Figure 2(c)→1(d); this involves applying an average filter to the image, subtracting a blurred (un-sharp) version of the image from itself, and then adding the difference to the original image. Finally, the edges of the solid phase as detected by the X-ray microtomography are identified by applying a Sobel mask filter in combination with a Laplacian of Gaussian (LoG) filter in the two Cartesian directions, Figure 1(d)→(e). The use of the LoG, which is a form of second-derivative filter, is motivated by the fact that the Sobel filter is commonly misled by noise, creating false edges (Gonzalez et al., 2004). Application of the Sobel and LoG filter together leads to an image like that shown in Figure 2(e). As indicated by the red circles in this figure, there are still some solid areas whose size and location relative to others suggest they should not be stand-alone – these are dealt with in the next step of the method.

Step 2. Identifying particle cross sections in the cross-sectional images

If the spherical particles were well resolved, the solids regions revealed by Step 1 would be circular in nature. As Figure 2(e) shows, however, this does not occur for µPBs because the resolution of X-ray microtomography is limited relative to the particle sizes typical of µPBs. To address this issue, two successive operations are applied independently to all the cross-sectional images.

In the first of these operations, the solid regions in an image that are far from circular in nature are subdivided into a number of regions that each are sufficiently circular to be considered as part of a single particle. This is done by first evaluating the 'roundness' of each solid region within the image using the expression

$$R_{O_i} = 4\pi \frac{A_i}{P_i^2} \tag{1}$$

where P_i and A_i are the perimeter and area of the region-i, respectively. A perfect circle has a roundness of unity whilst, as seen in Figure 2(f), it takes on a value less than this for any other shape. Experimentation showed here that the roundness can be used to determine the number of particles merged within a single solid region such as those shown in Figure 1(g) as follows

$$1 \leq R_{O_i} \leq 0.65 \rightarrow \text{region} \in \text{single particle} \tag{2a}$$

$$0.65 < R_{O_i} \leq 0.4 \rightarrow \text{region} \in \text{two particles} \qquad (2b)$$

$$0.4 < R_{O_i} \leq 0.3 \rightarrow \text{region} \in \text{three particles} \qquad (2c)$$

$$0.3 < R_{O_i} < 0 \text{ region} \in \text{four particles} \qquad (2d)$$

The thresholds in these equations were determined by comparing the masked images and the original image obtained from X-ray microtomography, and evaluating their roundness parameters.

If any but condition (2a) applies for a region, Watershed segmentation using the distance transform is employed successively on the region and the 'off-spring' regions derived from it until their roundness falls within the condition (2a), Figure 2(g).

Once all solid regions within the image have been determined to belong to a single particle, the image is subject to the second operation in this step, which sees each region replaced by a circle centred at the centroid of the region, Figure 2(h). The circle radius is determined by matching the area of the region with that which is closest to the cross section selected from a sphere that has been sliced up into K segments ($K = d_p/R$) as illustrated in Figure 3, where d_p is the experimentally determined average diameter of the particles, and R is the inter-plane resolution of the X-ray microtomography machine used.
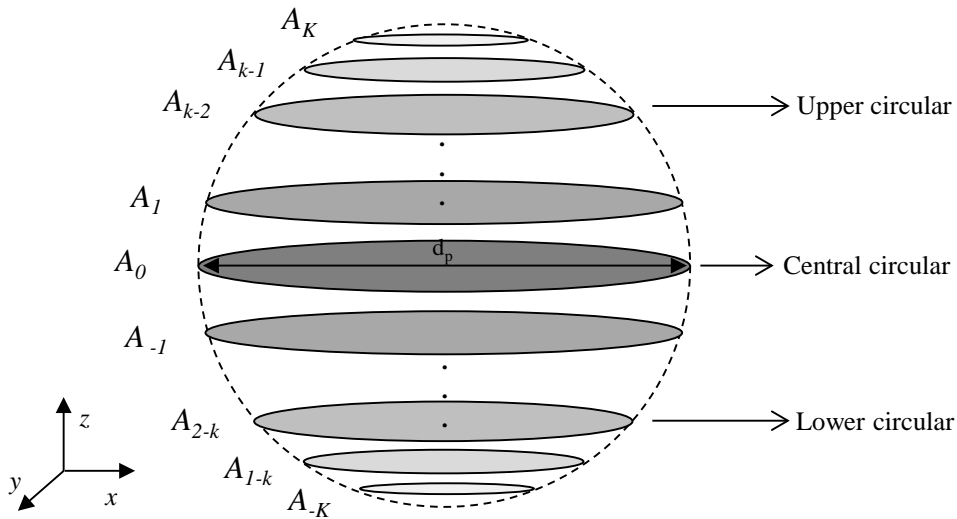
Figure 3. Partitioning of a spherical particle into sequential circular planes of area A_i for $i = 0, \pm 1$, …, $\pm K$, where $A_i = A_{-i}$.

Step 3. Initial reconstruction of the bed particles

This step sees all the particles in the µPB reconstructed by drawing correlations between circles in successive images (i.e. an image and that immediately below it), starting from the top-most image, as illustrated in Figure 2(i). The top of a new particle is identified in an image when a circle of area A_K (or A_{K-1} in recognition of the finite resolution) is detected, Figure 3. Appropriate circles in the

successive images are added to the particle until its bottom is detected, which occurs when a second circle of area A_K (or, if this is not detected, A_{K-1}, in recognition of the finite resolution) is detected after passing through circles of initially increasing and then decreasing area with a maximum in between of A_0.

Step 4. Estimating the centroid of the bed particles

For each particle, i, in the µPB the coordinates of its centroid are finally estimated by applying triangulation to the slices identified for the particle

$$X_i = \frac{\sum_{j=1}^{K} x_j}{K} \tag{3a}$$

$$Y_i = \frac{\sum_{j=1}^{K} y_j}{K} \tag{3b}$$

$$Z_i = \frac{\sum_{j=1}^{K} z_j}{K} \tag{3c}$$

where

$$x_j = \left(\frac{(x_j^l z_{-j}^0 - z_j^0 x_{-j}^r)(x_{-j}^l - x_j^r) - (x_j^l - x_{-j}^r)(x_{-j}^l z_j^0 - z_{-j}^0 x_j^r)}{(x_j^l - x_{-j}^r)(z_{-j}^0 - z_j^0) - (z_j^0 - z_{-j}^0)(x_{-j}^l - x_j^r)} \right) \tag{3d}$$

$$y_j = \left(\frac{(x_j^l z_{-j}^0 - z_j^0 x_{-j}^r)(y_{-j}^l - y_j^r) - (y_j^l - y_{-j}^r)(x_{-j}^l z_j^0 - z_{-j}^0 x_j^r)}{(x_j^l - x_{-j}^r)(z_{-j}^0 - z_j^0) - (z_j^0 - z_{-j}^0)(x_{-j}^l - x_j^r)} \right) \tag{3e}$$

$$z_j = \left(\frac{(x_j^l z_{-j}^0 - z_j^0 x_{-j}^r)(z_{-j}^l - z_j^r) - (z_j^l - z_{-j}^r)(x_{-j}^l z_j^0 - z_{-j}^0 x_j^r)}{(x_j^l - x_{-j}^r)(z_{-j}^0 - z_j^0) - (z_j^0 - z_{-j}^0)(x_{-j}^l - x_j^r)} \right) \tag{3f}$$

The $\left(x_j^m, y_j^m, z_j^m \right)$ in Equation (3d)-(3f) are the coordinates of the mth peripheral point on circle $j=1,...,K$ as illustrated in Figure 4 for the x-z plane. The uncertainty associated with these coordinates is also estimated in the form of the standard deviation from the average; this uncertainty is used in Part B. By continuing this procedure over the whole length of µPB, the 3D structure of packing will be obtained as presented in Figure 2(k).

4. Experimental details for demonstrating the new technique

The new technique is demonstrated here by using it to reconstruct the packing of near-monodisperse 30.5 µm particles of high sphericity within a square cross-sectioned micro-capillary and estimating the porosity which is compared to the actual porosity determined directly.
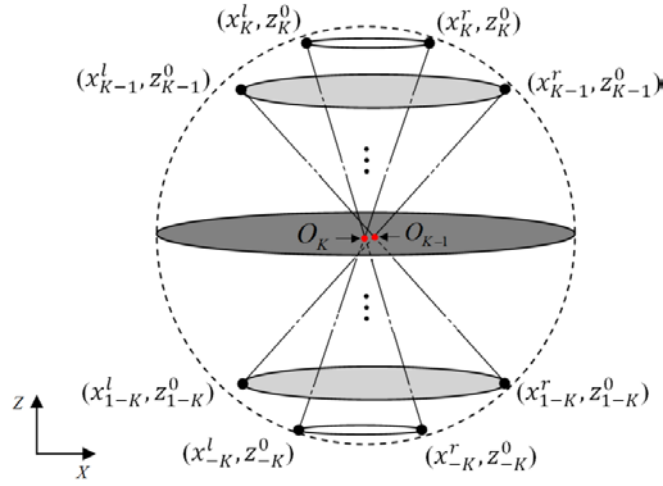
Figure 4. An illustration of the triangulation procedure in the *x-z* plane. The lines between the opposite edges of circles $\pm k$ intersect to yield an estimate of the sphere centroid O_k. The average centroid and the standard deviation (uncertainty) are derived from the set of these centroid points.

4.1. Experimental setup

The µPB was composed of a borosilicate micro-capillary of $D = 200$ µm internal square cross-section and 100 µm thick walls packed to a height of between 40-45 mm with soda-lime glass particles (Cospheric LLC; CA, USA) of average diameter $d_p = 30.5$ µm with a 1.5 µm standard deviation and sphericity of more than 95%. Figure 5(a) illustrates the method used to fill the µPB with the particles. A custom-built glass rig, details of which are provided in Figure 5(b), was used to connect a glass funnel to the top of the micro-capillary. The magnetic screws were embedded in the glass rig to attach the micro-packed capillaries and glass funnel to a steel base and make the experimental setup vertical. The micro-capillary was initially filled with ethanol before some of the particle-in-ethanol suspension was poured into it whilst being tapped to enhance particle settling. The bottom of the micro-capillary was embedded within a wickable surface (double sided adhesive tape), so as to quickly and effectively remove the ethanol used to initially suspend the glass particles from the micro-capillary, leaving behind the dry µPB of interest here. This process was repeated until the micro-capillary was filled to between 40-45mm deep.
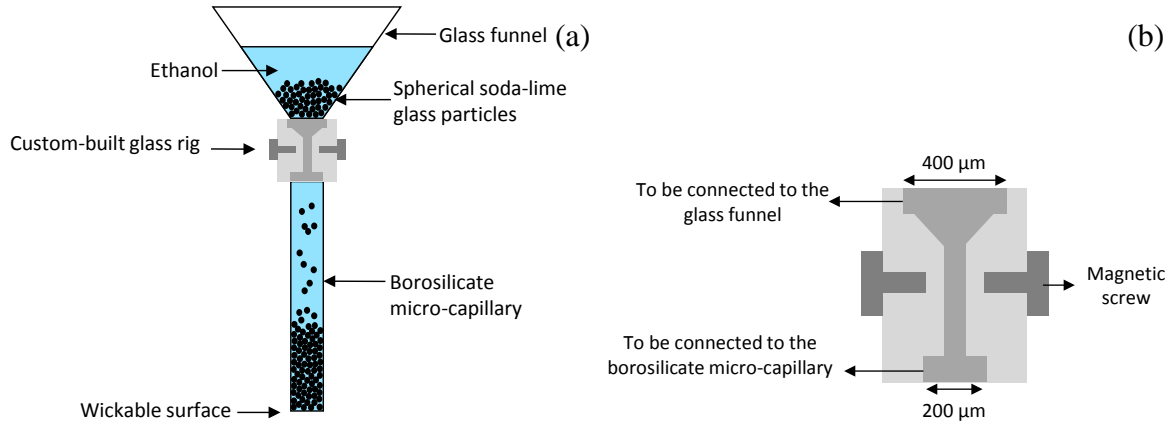
Figure 5. (a) Schematic of method for making micro-packed capillaries (µPBs) considered here; (b) the details of custom-built glass rig used for packing the µPB.

A SkyScan1072 X-ray microtomography system (SkyScan, Belgium) was used (see Table 1 for relevant details of this system and the scanning parameters for the study). The radiographic images were saved in TIFF format.

Table 1. The X-ray microtomography system and scanning parameters

Parameters	Value
In-plane and vertical spatial resolutions	2.28 µm
Angular rotation step	0.45 degree
Rotation step	180 degree
Magnification	137.17
Source (Tension/Current)	55/110 kV/µA
Exposure time	2.7 ms
Filter material	Al 0.5 mm
Frame averaging	3

4.2. Evaluating the porosity from the reconstructed µPB

The porosity of reconstructions of µPBs was estimated *via* Monte Carlo (MC) integration. This involves depositing M points randomly within a reconstructed packed bed and counting the number that fall within the particles, M_S, and then using

$$\phi_{MC} = 1 - M_S/M \tag{4}$$

In the study here, $M = 2450000$ points was found to give a stable estimate of the porosity. The final porosity estimate and its uncertainty were obtained from 10 repeats of the MC integration.

4.3. Direct measurement of the porosity of the µPB

The actual porosity of the µPB was determined directly by measuring the mass of the glass particles in the bed and converting this to a solid volume using the density of the glass (2500 kg/m^3), and then dividing by the total measured volume of the bed. The volume of the bed was set equal to the product of the cross sectional area of the micro-capillary and the height of the packing, which was measured with a precision of 15 µm using a microscope. The mass of the glass particles was estimated as the difference between average mass of the µPB and the empty micro-capillary, both

of which were measured using a high-precision balance (Sartorius AG Semi-microbalance, Germany; 0.01 mg precision). Their average mass in each case was that of ten separate measurements.

5. Results and Discussion

Figure 6(a) shows the cross-section obtained from the new method that corresponds to that shown in Figure 1. It is clear from this figure that the underlying spherical geometry is retained in the reconstruction. Figure 6(b) shows, however, that the 3D structure obtained *via* the new method includes some overlapping particles, which are shaded. This reflects the uncertainties associated with the identification of the centres of the particle cross-sections in each image as well as the assumption that the particles are spheres of identical size. These two issues will be addressed in Part B.
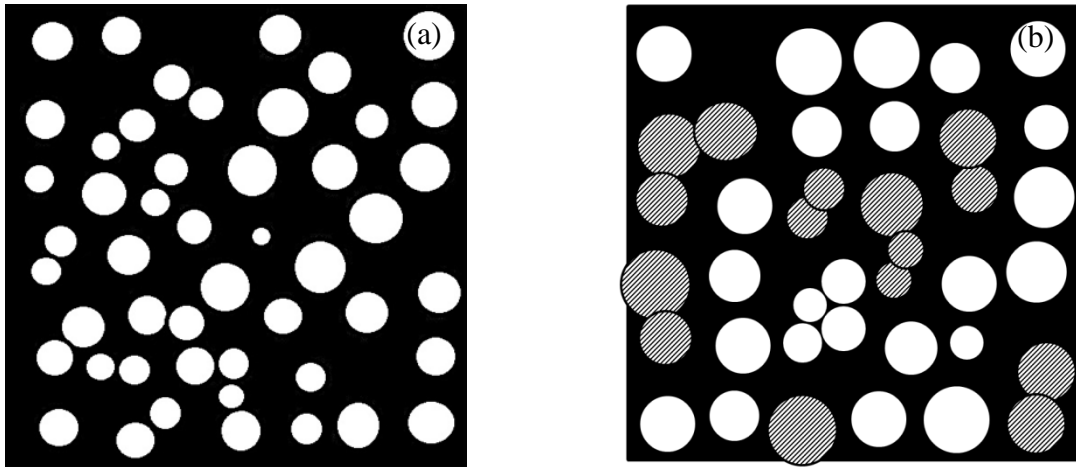

Figure 6. Cross-sections derived by applying the new method outlined here to two example cross-sections obtained in the work here: (a) the cross-section obtained from the image shown in Figure 1 where no particle overlap is observed; and (b) another cross-section that includes particles that overlap with each other and the bed walls (shaded circles) due to the reasons explained in the text.

Figure 7(a) shows the 3D reconstruction of the μPB considered here along with some close-ups of the model. Comparing this to the structure obtained using the traditional thresholding approach, Figure 7(b), clearly shows the new method described here retains the underlying spherical geometry whilst the traditional approach does not. Detailed inspection of the structure obtained by the new method reveals the differences in the particle packing between the wall and interior of the bed, compare Figure 7(c) and (d), something that is not the case from the traditional image as seen in Figure 7(e) and (f). Whilst the new method yields structures that are more intuitive, they are not perfect in that there are examples of where particles are overlapping each other or the micro-capillary wall, Figure 7(g) and (h), or are suspended in mid-air as seen in Figure 7(i).

As shown in Table 2, the porosity obtained from applying MC integration (ϕ_{MC}) over the reconstruction of the μPB is, within statistical uncertainty, the same as that obtained from the direct

measurement (ϕ_D). The same cannot be said, however, for the porosity obtained from applying MC integration to the reconstructions yielded through application of the Otsu automatic thresholding method (Otsu, 1979), which is one of the most widely used thresholding methods at present. In this case, the estimated porosity is around 9.7% lower, significantly outside the error margins associated with the direct measurement method. The assumption of monosize particle to find the porosity of μPB in this method induces an inherent deviation of around 7%.
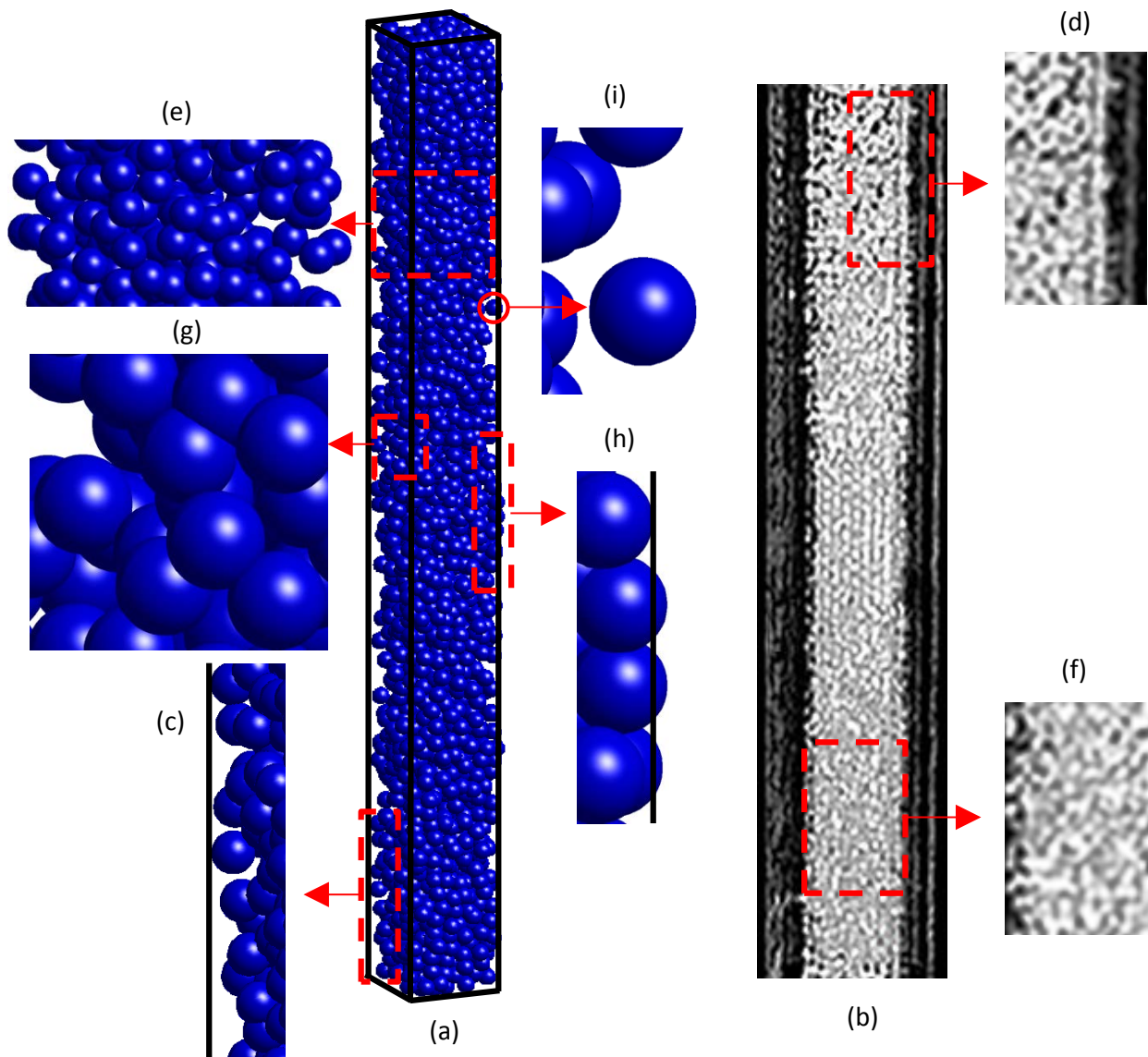

Figure 7. (a) 3D reconstruction of the μPB obtained from micro-CT images using the new approach outlined in this paper; (b) 3D reconstruction of the μPB obtained from micro-CT images using the traditional thresholding approach with a threshold of 75%; (c) close-up of the near wall region in the model shown in (a); (d) close-up of the near wall region in the model shown in (b); (e) close-up of the middle of the bed in the model shown in (a); (f) close-up of the middle of the bed in the model shown in (b); (g)-(i) close-ups showing, respectively, particle-particle overlap, particle-wall overlap, and a suspended particle in the model shown in (a).

$\phi_T{}^1$			$\phi_{MC}{}^2$	$\phi_D{}^3$
Manual		**Automatic**		
60%	70%	80%		
37.3	40.6	42.3	48.5±1.6	52±2

Table 2. Porosity values (%) obtained with different methods

1. Porosities derived from binarized images using different greyscale thresholds selected either manually or via the automatic Otsu method (Otsu, 1979).
2. Porosity derived from applying Monte Carlo integration to the model built using the new method described here.
3. Porosity obtained via direct measurement of the actual µPB.

As anticipated in the Introduction to this paper, Table 2 also reveals that when thresholding is used as a basis for reconstructing a model of the µPB, the porosity changes substantially with the threshold used. The increase in porosity with the threshold value is linear, with the rate being around 0.25% *per* percent-grayscale. Thus, using a greyscale threshold of 60%, the error in the voidage is around 15%, decreasing to around 10% for the threshold yielded by the Otsu automatic thresholding method (Otsu, 1979) (*i.e.* 80%).

Although the porosity yielded using the 3D structure obtained from the new method here cannot be statistically differentiated from the actual, it is lower than these values. This trend arises from the fact that the 3D structure yielded by the method includes overlapping particles, and particles overlapping with the micro-capillary walls as shown in Figure 7. This issue will be addressed in Part B. Although we have applied the new method to a µPB composed of near-monodisperse particles of high sphericity, it is conceivable that it can be applied to less-ideal beds. For example, dispersion in spherical particle sizes, including multimodal particle sizes could be considered by selecting appropriately from a library of circular cross-sections in Step 2, rather than just the one as done here, in conjunction with establishing cross-correlations between slices. Extension to beds composed of particles whose cross-sections are elliptical in nature is also possible if this is done provided the roundness metric in Equation (1) and the associated criteria in Equation (2) are generalised.

6. Conclusion

Whilst benchtop X-ray microtomography systems can yield three-dimensional (3D) images of the structure and porosity of packed beds, they are generally of poor quality when the beds are part of microfluidic devices due to the low resolution of the X-ray systems relative to the dimensions of the particles and porosity. This manifests as a loss of the underlying particle geometry and the conversion of the grayscale images into binary counterparts being sensitive to the greyscale threshold used to partition the pixels between the solid and void phases. A new method is described here that obviates both these issues when the micro-packed beds (µPBs) are composed of largely monodisperse particles of high sphericity. The method has been demonstrated by applying it to a

μPB. The recovered structure appears reasonable and has a porosity that is, within experimental uncertainty, equal to the value measured directly. In comparison, use of the well-known Otsu automatic thresholding method to partition the greyscale images into solid and void regions yielded a model in which the underlying spherical geometry and various other structural details were destroyed, and a porosity that was nearly 10% less than the actual. Whilst the new, alternative method described herein offers a major improvement over such commonly used methods, the monodispersity assumption and uncertainties associated with locating particle centres in the packing means anomalies are present in the models yielded here; for example, some overlapping particles. A method for addressing this issue is outlined in Part B of this work.

Acknowledgement

References

ABGRALL, P. & GUÉ, A. M. 2007. Lab-on-chip technologies: making a microfluidic network and coupling it into a complete microsystem—a review. *Journal of Micromechanics and Microengineering,* 17**,** R15.

AGGARWAL, P., TOLLEY, H. D. & LEE, M. L. 2012. Monolithic bed structure for capillary liquid chromatography. *Journal of Chromatography A,* 1219**,** 1-14.

AJMERA, S., DELATTRE, C., SCHMIDT, M. & JENSEN, K. 2001. A Novel Cross-Flow Microreactor for Kinetic Studies of Catalytic Processes. *In:* MATLOSZ, M., EHRFELD, W. & BASELT, J. (eds.) *Microreaction Technology.* Springer Berlin Heidelberg.

AL-RAOUSH, R. & ALSHIBLI, K. A. 2006. Distribution of local void ratio in porous media systems from 3D X-ray microtomography images. *Physica A: Statistical Mechanics and its Applications,* 361**,** 441-456.

ATWOOD, R. C., JONES, J. R., LEE, P. D. & HENCH, L. L. 2004. Analysis of pore interconnectivity in bioactive glass foams using X-ray microtomography. *Scripta Materialia,* 51**,** 1029-1033.

BOAS, F. E. & FLEISCHMANN, D. 2012. CT artifacts: causes and reduction techniques. *Imaging in Medicine,* 4**,** 229-240.

BROMLEY, E. H. C. & HOPKINSON, I. 2002. Confocal Microscopy of a Dense Particle System. *Journal of Colloid and Interface Science,* 245**,** 75-80.

BUZUG, T. M. 2008. *Computed tomography: from photon statistics to modern cone-beam CT*, Springer Science & Business Media.

CALVO, S., BEUGRE, D., CRINE, M., LÉONARD, A., MARCHOT, P. & TOYE, D. 2009. Phase distribution measurements in metallic foam packing using X-ray radiography and micro-tomography. *Chemical Engineering and Processing: Process Intensification,* 48**,** 1030-1039.

CAO, C., PALO, D. R., TONKOVICH, A. L. Y. & WANG, Y. 2007. Catalyst screening and kinetic studies using microchannel reactors. *Catalysis Today,* 125**,** 29-33.

CLAXTON, N. S., FELLERS, T. J. & DAVIDSON, M. W. 2006. Microscopy, Confocal. *Encyclopedia of Medical Devices and Instrumentation.* John Wiley & Sons, Inc.

COURTOIS, J., SZUMSKI, M., GEORGSSON, F. & IRGUM, K. 2006. Assessing the Macroporous Structure of Monolithic Columns by Transmission Electron Microscopy. *Analytical Chemistry,* 79**,** 335-344.

DAUTZENBERG, F. & MUKHERJEE, M. 2001. Process intensification using multifunctional reactors. *Chemical Engineering Science,* 56**,** 251-267.

DESTEFANO, J., LANGLOIS, T. & KIRKLAND, J. 2008. Characteristics of superficially-porous silica particles for fast HPLC: some performance comparisons with sub-2-µm particles. *Journal of chromatographic science,* 46**,** 254-260.

DING, M., ODGAARD, A. & HVID, I. 1999. Accuracy of cancellous bone volume fraction measured by micro-CT scanning. *Journal of Biomechanics,* 32**,** 323-326.

DOROODCHI, E., PENG, Z., SATHE, M., ABBASI-SHAVAZI, E. & EVANS, G. M. 2012. Fluidisation and packed bed behaviour in capillary tubes. *Powder Technology,* 223**,** 131-136.

DOROODCHI, E., SATHE, M., EVANS, G. & MOGHTADERI, B. 2013. Liquid–liquid mixing using micro-fluidised beds. *Chemical Engineering Research and Design,* 91**,** 2235-2242.

DULAY, M. T., KULKARNI, R. P. & ZARE, R. N. 1998. Preparation and Characterization of Monolithic Porous Capillary Columns Loaded with Chromatographic Particles. *Analytical Chemistry,* 70**,** 5103-5107.

EHRFELD, W., HESSEL, V. & LÖWE, H. 2000. *Microreactors: New Technology for Modern Chemistry*, Wiley.

FAJARDO, R. J., RYAN, T. M. & KAPPELMAN, J. 2002. Assessing the accuracy of high-resolution x-ray computed tomography of primate trabecular bone by comparisons with histological sections. *American Journal of Physical Anthropology,* 118**,** 1-10.

FU, X., DUTT, M., BENTHAM, A. C., HANCOCK, B. C., CAMERON, R. E. & ELLIOTT, J. A. 2006. Investigation of particle packing in model pharmaceutical powders using X-ray microtomography and discrete element method. *Powder Technology,* 167**,** 134-140.

GONZÁLEZ, R. C. & WOODS, R. E. 2008. *Digital Image Processing*, Pearson/Prentice Hall.

GONZALEZ, R. C. A., WOODS, R. E. A. & EDDINS, S. L. A. 2004. *Digital image processing: using MATLAB*, Prentice Hall.

HAEBERLE, S., MARK, D., VON STETTEN, F. & ZENGERLE, R. 2012. Microfluidic Platforms for Lab-On-A-Chip Applications. *In:* ZHOU, Z., WANG, Z. & LIN, L. (eds.) *Microsystems and Nanotechnology.* Springer Berlin Heidelberg.

HARA, T., TANCK, E., HOMMINGA, J. & HUISKES, R. 2002. The influence of microcomputed tomography threshold variations on the assessment of structural and mechanical trabecular bone properties. *Bone,* 31**,** 107-109.

HO, S. T. & HUTMACHER, D. W. 2006. A comparison of micro CT with other techniques used in the characterization of scaffolds. *Biomaterials,* 27**,** 1362-1376.

HOTZ, N., OSTERWALDER, N., STARK, W. J., BIERI, N. R. & POULIKAKOS, D. 2008. Disk-shaped packed bed micro-reactor for butane-to-syngas processing. *Chemical Engineering Science,* 63**,** 5193-5201.

JAECQUES, S. V. N., VAN OOSTERWYCK, H., MURARU, L., VAN CLEYNENBREUGEL, T., DE SMET, E., WEVERS, M., NAERT, I. & VANDER SLOTEN, J. 2004. Individualised, micro CT-based finite element modelling as a tool for biomechanical analysis related to tissue engineering of bone. *Biomaterials,* 25**,** 1683-1696.

JENSEN, K. F. 2001. Microreaction engineering — is small better? *Chemical Engineering Science,* 56**,** 293-303.

JONES, A. C., MILTHORPE, B., AVERDUNK, H., LIMAYE, A., SENDEN, T. J., SAKELLARIOU, A., SHEPPARD, A. P., SOK, R. M., KNACKSTEDT, M. A., BRANDWOOD, A., ROHNER, D. & HUTMACHER, D. W. 2004. Analysis of 3D bone ingrowth into polymer scaffolds via micro-computed tomography imaging. *Biomaterials,* 25**,** 4947-4954.

JUNG, S., EHLERT, S., MORA, J.-A., KRAICZEK, K., DITTMANN, M., ROZING, G. P. & TALLAREK, U. 2009. Packing density, permeability, and separation efficiency of packed microchips at different particle-aspect ratios. *Journal of Chromatography A,* 1216**,** 264-273.

KETCHAM, R. A. & CARLSON, W. D. 2001. Acquisition, optimization and interpretation of X-ray computed tomographic imagery: applications to the geosciences. *Computers & Geosciences,* 27**,** 381-400.

KIWI-MINSKER, L. & RENKEN, A. 2005. Microstructured reactors for catalytic reactions. *Catalysis Today,* 110**,** 2-14.

LIANG, C., DAI, S. & GUIOCHON, G. 2003. A Graphitized-Carbon Monolithic Column. *Analytical Chemistry,* 75**,** 4904-4912.

LIM, K. S. & BARIGOU, M. 2004. X-ray micro-computed tomography of cellular food products. *Food Research International,* 37**,** 1001-1012.

LOSEY, M. W., SCHMIDT, M. A. & JENSEN, K. F. 2001. Microfabricated Multiphase Packed-Bed Reactors: Characterization of Mass Transfer and Reactions. *Industrial & Engineering Chemistry Research,* 40**,** 2555-2562.

MAN, W., DONEV, A., STILLINGER, F. H., SULLIVAN, M. T., RUSSEL, W. B., HEEGER, D., INATI, S., TORQUATO, S. & CHAIKIN, P. M. 2005. Experiments on Random Packings of Ellipsoids. *Physical Review Letters,* 94**,** 198001.

MELIN, J. & QUAKE, S. R. 2007. Microfluidic Large-Scale Integration: The Evolution of Design Rules for Biological Automation. *Annual Review of Biophysics and Biomolecular Structure,* 36**,** 213-231.

MILLS, P. L., QUIRAM, D. J. & RYLEY, J. F. 2007. Microreactor technology and process miniaturization for catalytic reactions—A perspective on recent developments and emerging technologies. *Chemical Engineering Science,* 62**,** 6992-7010.

MITTON, D., CENDRE, E., ROUX, J. P., ARLOT, M. E., PEIX, G., RUMELHART, C., BABOT, D. & MEUNIER, P. J. 1998. Mechanical Properties of Ewe Vertebral Cancellous Bone Compared With Histomorphometry and High-Resolution Computed Tomography Parameters. *Bone,* 22**,** 651-658.

MOTOKAWA, M., KOBAYASHI, H., ISHIZUKA, N., MINAKUCHI, H., NAKANISHI, K., JINNAI, H., HOSOYA, K., IKEGAMI, T. & TANAKA, N. 2002. Monolithic silica

columns with various skeleton sizes and through-pore sizes for capillary liquid chromatography. *Journal of Chromatography A,* 961**,** 53-63.

OLESCHUK, R. D., SHULTZ-LOCKYEAR, L. L., NING, Y. & HARRISON, D. J. 2000. Trapping of bead-based reagents within microfluidic systems: on-chip solid-phase extraction and electrochromatography. *Analytical chemistry,* 72**,** 585-590.

OTSU, N. 1979. A Threshold Selection Method from Gray-Level Histograms. *Systems, Man and Cybernetics, IEEE Transactions on,* 9**,** 62-66.

PAL, N. R. & PAL, S. K. 1993. A review on image segmentation techniques. *Pattern Recognition,* 26**,** 1277-1294.

PLUMMER, C. J. G., HILBORN, J. G. & HEDRICK, J. L. 1995. Transmission electron microscopy methods for the determination of void content in polyimide thin film nanofoams. *Polymer,* 36**,** 2485-2489.

RASBAND, W. S. 1997-2013. ImageJ. U. S. National Institutes of Health, Bethesda, Maryland, USA (http://imagej.nih.gov/ij/).

REYES, D. R., IOSSIFIDIS, D., AUROUX, P. A. & MANZ, A. 2002. Micro total analysis systems. 1. Introduction, theory, and technology. *Analytical chemistry,* 74**,** 2623-2636.

SAGE, D., PRODANOV, D., TINEVEZ, J.-Y. & SCHINDELIN, J. 2012. MIJ: Making Interoperability Between ImageJ and Matlab Possible. *ImageJ User & Developer Conference.* Luxembourg.

SALVO, L., CLOETENS, P., MAIRE, E., ZABLER, S., BLANDIN, J. J., BUFFIÈRE, J. Y., LUDWIG, W., BOLLER, E., BELLET, D. & JOSSEROND, C. 2003. X-ray micro-tomography an attractive characterisation technique in materials science. *Nuclear Instruments and Methods in Physics Research Section B: Beam Interactions with Materials and Atoms,* 200**,** 273-286.

SCHULTE, T. H., BARDELL, R. L. & WEIGL, B. H. 2002. Microfluidic technologies in clinical diagnostics. *Clinica Chimica Acta,* 321**,** 1-10.

SEDERMAN, A. J., ALEXANDER, P. & GLADDEN, L. F. 2001. Structure of packed beds probed by Magnetic Resonance Imaging. *Powder Technology,* 117**,** 255-269.

SEZGIN, M. & SANKUR, B. L. 2004. Survey over image thresholding techniques and quantitative performance evaluation. *Journal of Electronic Imaging,* 13**,** 146-168.

SHEN, H., NUTT, S. & HULL, D. 2004. Direct observation and measurement of fiber architecture in short fiber-polymer composite foam through micro-CT imaging. *Composites Science and Technology,* 64**,** 2113-2120.

SHEPPARD, A. P., SOK, R. M. & AVERDUNK, H. 2004. Techniques for image enhancement and segmentation of tomographic images of porous materials. *Physica A: Statistical Mechanics and its Applications,* 339**,** 145-151.

SUZUKI, M., OJIMA, K., IIMURA, K. & HIROTA, M. 2004. Measurement of Vertical Voidage Distribution in Powder Packed Bed Using X-ray Micro Computed Tomography-Comparison between Piston Compression and Centrifugal Compression. *J. Soc. Powder Technol., Japan,* 41**,** 663-667.

SUZUKI, M., SHINMURA, T., IIMURA, K. & HIROTA, M. 2008. Study of the wall effect on particle packing structure using X-ray micro computed tomography. *Advanced Powder Technology,* 19**,** 183-195.

UNGER, K. K., SKUDAS, R. & SCHULTE, M. M. 2008. Particle packed columns and monolithic columns in high-performance liquid chromatography-comparison and critical appraisal. *Journal of Chromatography A,* 1184**,** 393-415.

WAARSING, J. H., DAY, J. S. & WEINANS, H. 2004. An Improved Segmentation Method for In Vivo μCT Imaging. *Journal of Bone and Mineral Research,* 19**,** 1640-1650.

WILLIAMS, R. A. & JIA, X. 2003. Tomographic imaging of particulate systems. *Advanced Powder Technology,* 14**,** 1-16.

WONHO, O. & LINDQUIST, B. 1999. Image thresholding by indicator kriging. *Pattern Analysis and Machine Intelligence, IEEE Transactions on,* 21**,** 590-602.

ZIVKOVIC, V., BIGGS, M. J. & ALWAHABI, Z. T. 2013a. Experimental study of a liquid fluidization in a microfluidic channel. *AIChE Journal,* 59**,** 361-364.

ZIVKOVIC, V., KASHANI, M. & BIGGS, M. Experimental and theoretical study of a micro-fluidized bed. POWDERS AND GRAINS 2013: Proceedings of the 7th International Conference on Micromechanics of Granular Media, 2013b. AIP Publishing, 93-96.